Displays 76 (2023) 102343

Contents lists available at ScienceDirect

Displays

journal homepage: www.elsevier.com/locate/displa

X-ray image analysis for osteoporosis diagnosis: From shallow to deep analysis☆

Meriem Mebarkia [a], Abdallah Meraoumia [b,*], Lotfi Houam [b], Seddik Khemaissia [a]

[a] Laboratoire de Génie Electrique (LABGET), Larbi Tebessi University – Tebessa, Algeria
[b] LAboratory of Mathematics, Informatics and Systems (LAMIS), University of Larbi Tebessi, Tebessa, Algeria

ARTICLE INFO

Keywords:
Osteoporosis
Feature extraction
Deep analysis
Gabor filter
HOG
LPQ
Bat algorithm

ABSTRACT

Recently, automated disease diagnosis based on medical images has become an integral component of digital pathology packages. Texture analysis is commonly used to address this issue, particularly in the context of estimating the osteoporosis progression in bone samples. Most research in this context uses handcrafted methods to directly extract bones image features despite the substantial correlation between sick and healthy bones, which explains the limited results. In this work, the handcrafted feature extraction method (e.g. HOG and/or LPQ) will be applied to a set of descriptors obtained from a deep analysis of bone texture images using Gabor's filter bank. In addition, the classifier automatically adjusts the Gabor filters settings, using the bat-inspired algorithm based optimization, to achieve deep analysis behavior and optimal performance. Using a typically osteoporosis database, our experimental results reveal a significant improvement over the state-of-the-art deep/handcrafted techniques, resulting in an excellent performance of 89.66% for osteoporosis diagnosis.

1. Introduction

In 1895, *Roentgen* [1] may have been the first to notice that X-rays could be used to acquire an image of the organs inside the human body, from which one could determine whether or not there was disease. Since then, medical imaging using X-rays has become an important diagnostic tool for a variety of diseases. In fact, information extracted from images plays an important role in decision-making at many stages of patient care, including detection, characterization, staging, evaluation of treatment response, follow-up and evaluation of residual and recurrent disease after treatment, and surgery and radiotherapy guidance [2]. Despite the incredible development of medical imaging devices, the analysis and interpretation of captured images remains a major challenge for radiologists, because any error in interpretation can lead to the prescription of the wrong drugs, thus putting the patient in danger and destroying the success of the treatment. For example, on mammogram images, it can be difficult for radiologists, with a subjective examination, to distinguish between a tumor and a calcification. It is also difficult for them to detect with the naked eye the presence of a tumor in the dense breast [3]. Due to the inexperience of many radiologists and the large number of cases reviewed periodically, the treatment process will be expensive due to the large number of errors. So, to avoid or cut down on diagnostic mistakes, radiologists need a way to help them make the right decisions. Soft computing paradigms are a good way to do this.

Medical devices have recently played a significant role in the improvement of the standard of medical diagnostics thanks to technological improvements in both hardware and software. Therefore, hospitals have worked in recent years to take advantage of various technologies to raise the quality of healthcare and boost efficiency while reducing errors. Indeed, diagnosis through the use of medical imaging has been one of the areas that has substantially benefited from the development of technology, as medical companies have worked in recent years to produce medical imaging devices of high quality that give very accurate results. X-ray imaging is one of the most widely used medical imaging techniques, giving doctors an image of the interior organs of the human body without the requirement for surgery [4]. Numerous pathologies, like osteoporosis, can indeed be detected and treated by utilizing X-ray imaging-based diagnosis.

Osteoporosis is a common bone disease that frequently results in disability, particularly in the elderly [5]. This disease is directly caused

☆ This paper was recommended for publication by Prof Guangtao Zhai.

* Corresponding author.
E-mail addresses: meriem.mebarkia@univ-tebessa.dz (M. Mebarkia), ameraoumia@univ-tebessa.dz (A. Meraoumia), lotfi.houam@univ-tebessa.dz (L. Houam), seddikk@hotmail.com (S. Khemaissia).

https://doi.org/10.1016/j.displa.2022.102343
Received 22 August 2022; Received in revised form 21 November 2022; Accepted 24 November 2022
Available online 5 December 2022

by low bone mineral density and micro-architectural deterioration of bone tissue. Currently, in addition to clinical examinations, the detection of this disease using X-ray imaging, despite its limited clinical use, is one of the most important trends for assisting doctors in making correct decisions regarding the presence and evolution of this disease. In this context, numerous researchers have developed computer-assisted bone image analysis techniques to aid in the diagnosis of this disease. Unfortunately, the largest challenge is that the images taken from a patient with osteoporosis are extremely similar to those taken from healthy subjects, making classification difficult [6]. In spite of this, encouraging and promising results have been obtained to continue research in this field. Theoretically, images of diseased and healthy bone can be distinguished using supervised machine learning approaches that rely primarily on image texture analysis. This trait provides a variety of data that can be used to distinguish images and classify them successfully. Indeed, in examining the amount of bone loss and, therefore, the possibility of osteoporosis, the size and density of texture lines is one of the most crucial factors. In this work, before applying the handcrafted feature extraction method directly to the raw image, it will be thoroughly analyzed using a specific set of Gabor filters [7]. These filters extract multiple orientations of lines, which are then combined into a single descriptor. Next, two handcrafted feature extraction algorithms (Histogram of Oriented Gradient (HOG) [8] and Local Phase Quantization (LPQ) [9]) will be applied to the resulting descriptor. Also, the classifier optimizes the Gabor filter settings using optimization based on a bat-inspired algorithm in order to obtain optimal performance and deep analysis behavior. In addition, the proposed method can operate on the multimodality principle by fusing HOG and LPQ data or a texture analysis based on several distinct filter sizes. Using the dataset from the IEEE-ISBI Challenge: Characterization of Bone Tissue [10], experimental results show that the deep texture analysis approach for bone images is significantly more accurate than previous researches.

The remainder of this paper is organized as follows: In Section 2, a brief overview of osteoporosis is provided. Section 3 provides an overview of relevant research. In Section 4, the concept of our proposed methodology is presented. Using a public database, we evaluate the proposed method in Section 5. The aim of Section 6 is to discuss the results and compare them to some of the most recent approaches in the literature. Finally, Section 7 concludes the paper and presents future research.

2. Osteoporosis overview

The most prevalent bone disease in humans and a recognized serious public health issue is osteoporosis. Low bone density, deterioration of the micro-architecture of bone tissue, increased bone fragility, and a propensity to fracture are all symptoms of this disease, which affects the skeleton (Fig. 1).

Indeed, it can be estimated that approximately 50% of women and 20% of men will develop osteoporotic fractures during their lifetime [11]. For this reason, osteoporosis screening to avoid bone fractures in women over 65 has been advised by the American Working Group on Preventive Services [12]. Indeed, early diagnosis of osteoporosis is important in preventing fractures due to the effectiveness of treatment in the early stages of the disease before fractures occur [13]. Currently, assessment of Bone Mineral Density (BMD) of the proximal thigh and lumbar spine, by Dual-energy X-ray Absorptiometry (DXA, or DEXA) [14], is the most appropriate test for detecting osteoporosis.

3. Related works

The promising results obtained by analyzing the texture of X-ray images in the medical field and specifically in the diseases diagnosis are one of the most important factors that have led to the popularity of this technology and, consequently, its adoption as one of the most important factors in the diagnosis and treatment of numerous diseases, particularly osteoporosis. Recently, many works have been proposed in this regard, especially those related to the challenge of Texture Characterization of Bone radiograph images (TCB) [10] for the diagnosis of osteoporosis. In this section, we will discuss a selection of these interesting works, focusing on those that relate to the challenge noted above.

3.1. Current directions

With the advent of deep learning technology and its positive impact on pattern recognition systems, *Ran et al.* [15] evaluated the effectiveness of this technology in an osteoporosis diagnostic system. In fact, the model presented by the authors is mainly based on the fusion of deep and handcrafted features. To extract deep features, transfer learning principle based on four famous CNN architectures (*AlexNet* [16], *VggNet* [17], *ResNet* [18] and *DenseNet* [19]) was used while all features extracted using Grey Level Co-occurrence Matrix (GLCM) [20] and the Local Binary Pattern (LBP) [21] methods, as well as the encrypted version of the obtained features, were used as handcrafted features. The system performance was evaluated in both single-source and multiple-source scenarios. Experimental results have demonstrated that fusing *AlexNet* features with encoded features or all handcrafted features achieves the highest of accuracy (77.5%) compared to all other fusion combinations.

In [22], *Devendra et al.* proposed a multifractal method to characterize trabecular bone texture containing three basic steps. The first step is to calculate the Holder exponents [23] for each pixel in the X-ray image. In the second step, the Hausdorff dimensions [24] are determined from the Holder exponents which determine the global regularity of the pixels. In the last step, the lacunarity is estimated from the Hausdorff dimensions. After comparing the experimental results with the latest methods participating in the TCB challenge, the lacunarity plots [25] and the classification results show that the characterization of global regularity using Hausdorff dimensions significantly improved the characterization of trabecular bone texture and therefore osteoporosis classification performance.

In [26], *Ran Su el al.* proposed two new feature groups, encoded-GLCM and encoded-LBP, each of which consists of two subgroups by encoding Gabor and Hessian information [27]. Along with the original feature group (GLCM and LBP features), these two feature groups were classified into distinct groups and utilized to train the Random Forest classifier [28]. In this study, the performance of each feature was evaluated separately, and Recursive Feature Elimination (RFE) [29] was

Fig. 1. Healthy and osteoporotic bone architecture. *(a)* Healthy bone, and *(b)* Osteoporotic bone.

used to enhance efficiency. The inter and intra-groups/sub-groups results show that the GLCM-encoded and LBP-encoded features are more discriminate than the raw GLCM and LBP features. Thus, the optimal feature (LBP encoded group) can achieve up to 70% accuracy. In addition, this accuracy is increased to 71% by using only ten features.

In the work of *Keni Zheng et al.* [30], high-dimensional textural representations and the feature selection principle were used to obtain a more discriminating subset, which was then classified using four classifiers (Naive Bayes [31], Multilayer Perceptron [32], Bayes Network [33], Random Forests). In this work, five handcrafted feature extraction methods were used, namely wavelet decomposition [34], discrete Fourier/cosine transforms [35], fractal dimension [36], statistical co-occurrence indices and structural texture descriptors. The experimental results proved the efficiency of the system since it gave an accuracy of 79.3%.

Compared to the standard Bag-of-Visualwords (BoW) [37] model, Fisher's encoding [38] is more discriminating in representing the distribution of local descriptors in addition to occurrence frequencies. So, based on the above, *Yang Song et al.* [39] proposed a bone tissue characterization method based on the incorporation of an Improved Fisher Vector (IFV) into the BoW model. In this study, the authors extend the original IFV, which is based on Scale-Invariant Feature Transform (SIFT) [40], to include LBP. The system was evaluated on the 2014 ISBI challenge dataset [10] for characterization of bone texture, and the results showed excellent classification performance compared to previous work.

In [41], *Florian Yger et al.* uses simple feature types based on Covariance Matrices and Wavelet Marginals. Thus, covariance matrices were camputed from gradient and Gabor techniques (Gabor-based minimum covariance (CmdMat-grad) and gradient-based minimum covariance (CovMat-gab)). The experimental results showed a remarkable superiority of the method based on Wavelet Marginal.

3.2. Research purpose

In osteoporosis, the lines and/or pores of the bone image are unstable and vulnerable to significant changes, especially as the disease progresses (In images of healthy bones, the density of the lines increases and that of the pores decreases, whereas in images of diseased bones, the opposite occurs). Therefore, the information produced by these features is extremely reliable and can effectively diagnose the progression of this disease. Since a high degree of similarity between healthy and diseased bone is inevitable and has a significant impact on every step of osteoporosis diagnosis, it is important to focus exclusively on these features. The most significant limitations of previous research in the osteoporosis diagnosis are the inefficient use of bone image lines and/or pores. Focusing solely on texture analysis without considering these factors can result in feature vectors with a significant degree of interclass correlation. Based on this principle and to produce distinctive features, our proposed method is characterized by: ***(i)*** Extraction of lines and/or pores in several directions (orientations), ***(ii)*** Automatic adjustment of method parameters to a variety of conceivable cases (e.g. lines of different thicknesses), ***(iii)*** Analysis at several levels, and ***(iv)*** Ability to perform various bone images analyzes and then combines the results to make an informed decision.

4. Material and methods

4.1. Dataset

Our 174-subject dataset came from the IEEE-ISBI Challenge: Characterization of Bone Tissue [10]. This dataset has three 58-subject galleries. Osteoporotic subjects (OP, Osteoporotic patients) and control subjects (CT, Healthy people) are found in the first and second galleries, respectively, while the third gallery comprises an equal combination of OP patients and CT subjects. Each subject is a 16-bit bone X-ray image, with a size of 400 × 400 pixels. These images were used to evaluate the texture analysis techniques of our proposal.

4.2. Texture descriptors

To describe the texture of bone X-ray images, we have proposed a convolution based deep analysis method. All images were initially preprocessed to improve bone image contrast. In the following, we will detail the techniques used in the proposed method.

4.2.1. Theoretical aspects

This part allows us to describe preliminary requirements that will be used in the proposed texture analysis process.

- **Gabor filter bank:** The impulse response of a Gabor filter [42] is a sinusoidal function multiplied by a Gaussian function. So, in discrete space, the $N_x \times N_y$-sized 2-D complex Gabor filter is:

$$G_{(\theta,f_0,\gamma,\eta,\phi)}(x,y) = \frac{\gamma \bullet \eta}{\pi} e^{-\left((\alpha x_r)^2+(\beta x_r)^2\right)} e^{j2\pi f_0(x_c cos\theta + y_c sin\theta + \phi)}, \text{ with } \alpha = \frac{f_0}{\gamma}, \quad \beta = \frac{f_0}{\eta} \tag{1}$$

where θ, f_0 and ϕ denote the sinusoid rotation angle, digital frequency, and carrier phase, respectively. Also, γ and η are the normalized scale factors of the along-wave envelope and the wave-orthogonal Gaussian envelope, respectively. And.

$$\begin{cases} (x_c, y_c) = (x - x_0, y - y_0), \quad (x_0, y_0) = \left(\frac{N_x}{2}, \frac{N_y}{2}\right) \\ x_r = x_c cos\theta + y_c sin\theta \\ y_r = -x_c cos\theta + y_c \sin \end{cases} \tag{2}$$

The Gabor filter has several interesting properties, including invariance against illumination, rotation, scale, and translation. In addition to these properties, Gabor filters are localized in the spatial and frequency domain, which makes them perfectly suited for wavelet analysis. In practice, filter banks [43] are comprised of many Gabor filters, which constitute a *Gabor space*. This space employs the same principles as the human visual cortex, enabling the rapid detection of complex visual patterns. Taking Eq. (1) as a reference, the set of $\mathscr{K}$-component Gabor filters, $\mathscr{W}$, is thus defined as follows:

$$\mathscr{W}_{(n,m)}(x,y) = G_{(\theta_m, f_{0n}, \gamma, \eta)}(x,y)/\phi = 0 \tag{3}$$

Where $\mathscr{K} = K_s \bullet K_o$ is the number of Gabor filters, K_s and K_o are the numbers of scales and orientations, respectively, and.

$$\begin{cases} f_{0n} = \dfrac{f_0}{\left(\sqrt{2}\right)^{n-1}}, \quad n = 1, \cdots, K_s \\ \theta_m = (m-1)\dfrac{\pi}{K_o}, \quad m = 1, \cdots, K_o \end{cases} \tag{4}$$

Also, α and β are calculated, for each component (each scale), as follows:

$$(\alpha_n, \beta_n) = \left(\frac{f_{0n}}{\gamma}, \frac{f_{0n}}{\eta}\right) \tag{5}$$

Gabor filter set, $\mathscr{W}$, is the set of components for each set of Gabor filter size (square), sine angle (θ_m), and digital frequency (f_{0n}), which must be chosen empirically to better describe bone line details.

- **HOG descriptor:** Histogram of Oriented Gradient (HOG) [44] descriptors is like an edge map, but it stores both the gradient magnitude information and the cell-level edge locations. The location coarseness and normalization of HOG features are crucial because they provide some degree of invariance to small geometric and photometric changes. Assume that the input is the $H \times W$-sized

window I of a grayscale image, or even the whole image, to create a HOG feature, we follow the steps:

Calculate gradients: Find the components of the gradient (I_x, I_y) by:

$$\begin{cases} I_x(i,j) = I(i,j+1) - I(i,j-1) \\ I_y(i,j) = I(i-1,j) - I(i+1,j) \end{cases} \quad i = 1..H\,, \quad j = 1..W \tag{6}$$

The gradient is then transformed to polar coordinates with the angle limited between 0^o and 180^o degrees to identify opposite gradients.

$$\begin{cases} \mu = \sqrt{{I_x}^2 + {I_y}^2} \\ \theta = \dfrac{180}{\pi}\left(tan^{-1}(I_x, I_x) \mod \pi\right) \end{cases} \tag{7}$$

where tan^{-1} is the inverse tangent, which yields values between $-\pi$ and π, and μ and θ denote respectively the magnetitude and the direction (angle) of the gradient of each pixel.

Cell Orientation Histograms: The window is partitioned into non-overlapping neighboring $c \times c$-sized cells (*i.e.* $c = 8$). Then, for each cell, a histogram of the gradient directions sorted in B bins (*i.e.* $B = 9$) is calculated. Thus, the bins are numbered from 0 to $B-1$ and each has a width of $w = \frac{180}{B}$.

It is important to note that with so few bins, a pixel at a bin boundary could wind up in a different bin if the image changes significantly. Voting by bilinear interpolation is used to overcoming these quantization artifacts. This method lets each pixel in a cell contribute to two adjacent bins. This method divides the gradient magnitude between the two bins for each pixel based on the distance between the gradient orientation and the center of each bin. In other words, it calculates how much of the gradient magnitude is in each bin:

$$\mathscr{T}_{vote}(\mu_i, \theta_i, B_i, B_{i+1}) = \left\{ \begin{matrix} k_1\mu \to B_i \\ k_2\mu \to B_{i+1} \end{matrix} \middle/ k_1 + k_2 = 1 \right. \tag{8}$$

Since the gradient magnitude is always positive, the resulting cell histogram is a B-valued vector.

Block Normalization: In this phase, the cells are organized into overlapping $2c \times 2c$ pixel blocks with a vertical and horizontal overlapping step of c pixels. Next, the histograms of the four cells in each block are concatenated into a single block feature, which is then normalized using the Euclidean norm:

$$b_k = \left[h_{(i,j)}, h_{(i,j+1)}, h_{(i+1,j)}, h_{(i+1,j+1)}\right] \tag{9}$$

Where b_k denotes the feature of the block k and $h_{(i,j)}$ the histogram of the cell (i,j). This block feature is normalized as follows:

$$\widetilde{b}_k = \frac{b_k}{\sqrt{\|b_k\|^2 + \epsilon}} \tag{10}$$

Where ϵ is a small positive constant that prevents division by zero in gradient-free blocks.

HOG Feature: Lastly, to represent the whole window feature, all the normalized block features ($\widetilde{b}_k$) are concatenated to produce one HOG feature vector ($\mathscr{H}$), as shown below:

$$\mathscr{H} = \left[\widetilde{b}_1, \widetilde{b}_2, \cdots, \widetilde{b}_k, \cdots, \widetilde{b}_\rho\right] \tag{11}$$

Where ρ is the number of blocks in the window. Finally, the resulting HOG function is also normalized using Eq. (10).

- **LPQ descriptor:** Local Phase Quantization (LPQ) [45] extracts local phase information from a blurred image based on the blur invariance of Fourier phase response.

Local Frequency Analysis: LPQ operator on an image pixel is done by employing Short-term Fourier Transform (STFT) over a $M \times M$-sized window (W_n). Thus, for all pixel locations $x = \{x_1, x_2, ..., x_{HW}\}$ in an $H \times W$-sized image ($f(x)$), the local image patches in W_n are defined as follows:

$$f_x(y) = f(x - y)\,, \quad \forall y \in W_n \tag{12}$$

Applying STFT to W_n gives us the local frequency domain representation:

$$\mathscr{T}_x(u) = \sum_{y_i \in W_n} f_x(y_i) e^{-j2\pi u^T y_i} \tag{13}$$

where $i = 1, ..., M^2$. The variable u comprises ℓ frequency variables $(u_1, u_2, ...u_\ell)$ that serve as blur-insensitive local descriptors. The Eq. (13) can be rewritten as follows:

$$\mathscr{T}_x(u) = \psi_u^T \mathrm{f}_x\,, \quad \psi_u^T(y) = e^{-j2\pi u^T y} \tag{14}$$

Where.

$$\psi_u^T = [\psi_u(y_1), \psi_u(y_2), \cdots, \psi_u(y_{M^2})]\,, \quad \text{and} \quad \mathrm{f}_x = [f_x(y_1), f_x(y_2), \cdots, f_x(y_{M^2})] \tag{15}$$

To find the LPQ codeword, a phase quantization process is performed. Indeed, if the coefficients to be quantized are statistically independent, scalar quantization is performed directly; otherwise, the samples must be decorrelated before quantization.

Phase Quantization: The blur-insensitive representation uses ℓ frequencies, producing an ℓ-length feature vector for each pixel. In practice, the phase is quantized in four quadrants using the following quantizer:

$$\mathscr{Q}(\mathscr{T}_x(u)) = (\mathrm{Re}\{\mathscr{T}_x(u)\} > 0) + 2(\mathrm{Im}\{\mathscr{T}_x(u)\} > 0) \tag{16}$$

This quantization can be expressed with 2 bits per frequency for each pixel, for a total of 2ℓ bits; the concatenation of the codes for the ℓ frequency components results in a single codeword. To achieve a blur-insensitive representation, only low-frequency components are employed, as they contain the most of image energy. In practice, the local coefficients $\mathscr{T}_x$ are computed for each pixel at four low frequencies ($\ell = 4$):

$$[u_1, u_2, u_3, u_4] = \begin{bmatrix} a & 0 & a & a \\ 0 & a & a & -a \end{bmatrix} \tag{17}$$

The scalar a is the highest frequency whose point spread function (PSF) is positive and it is usually calculated from M (*i.e.* $a = \frac{1}{M}$). Finally, an 8-bit codeword ($[q_7, q_6, q_5, \cdots, q_0]$) can be obtained to describe the local texture surrounding each pixel (W_n). This codeword can easily be transformed into a decimal number (in the range 0–255) by simple binary decoding:

$$\mathrm{LPQ}_i = \sum_{j=1}^{8} q_j 2^{j-1} \tag{18}$$

Decorrelation: Vector quantization is typically more efficient in cases when the coefficients to be quantized are correlated. To decorrelate the frequency coefficients, we first separate the real and imaginary components of $\mathscr{T}_x(u)$ and then concatenate them as follows:

$$\mathscr{T}_x(u) = [\mathscr{T}_x(u_1), \mathscr{T}_x(u_2), \cdots, \mathscr{T}_x(u_\ell)] \tag{19}$$

$$\mathrm{F}_x = \left[\mathrm{Re}\{\mathscr{T}_x(u)\} \quad \mathrm{Im}\{\mathscr{T}_x(u)\}\right] = \left[\mathrm{F}_x^R \quad \mathrm{F}_x^I\right] \tag{20}$$

The STFT transform (Eq. (14)) shows that F_x and f_x are linearly dependent, so we can write:

$$\mathrm{F}_x = \Psi \cdot \mathrm{f}_x\,, \quad \text{where} \quad \Psi = \left[\Psi_\mathrm{R} \quad \Psi_\mathrm{I}\right]^\mathrm{T} \tag{21}$$

And.

$$\Psi_\mathrm{R} = \mathrm{Re}\left\{\left[\psi_{u_1}, \psi_{u_2}, \cdots, \psi_{u_\ell}\right]\right\} \quad \text{and} \quad \Psi_\mathrm{I} = \mathrm{Im}\left\{\left[\psi_{u_1}, \psi_{u_2}, \cdots, \psi_{u_\ell}\right]\right\} \tag{22}$$

To decorrelate F_x, *Ojansivu et al.* [46] applied the following transform:

$$G_x = V^T \cdot F_x \tag{23}$$

where V is an orthogonal matrix obtained from the matrix (D) mentioned below:

$$D = U\Sigma V^T \tag{24}$$

D is the covariance matrix of Fx and can be obtained by:

$$D = \Psi C \Psi^T \tag{25}$$

where C is the covariance matrix of $M \times M$ samples in W_n. After the decorrelation process, a scalar quantizer quantizes the j^{th} coefficient (g_j) of G_x:

$$q_j = \begin{cases} 1, & \text{if } g_j \geq 0 \\ 0, & \text{otherwise} \end{cases} \tag{26}$$

The resulting codeword is then transformed into a decimal number using the Equ.18. After computing the LPQ codewords for each pixel in the image, and since the LPQ range is 0 to 255, an image containing the LPQ information of the input image is produced. To calculate a feature vector ($\mathscr{H}$) for the input image in practice, we divide the LPQ image into non-overlapping $r \times c$-sized sub-regions and compute the histograms for each sub-region. Then, these histograms are concatenated to provide an LPQ feature vector for the whole input image.

$$\mathscr{H} = [h_1, h_2, \cdots, h_{rc}] \tag{27}$$

This division is used to keep some information about the spatial arrangement of the patterns, since the histograms of the whole image discard all of this information.

- **BAT Algorithm Optimization:** The goal of optimization is to find the best solution or to run a system as efficiently as possible. So, it is the process of adjusting the input data (decision variables) to obtain the best solution (minimum/maximum) for the actual problem. Indeed, metaheuristic approaches outperform precise ones because they more effectively explore and select attractive parts of the search space, especially from a computational standpoint. Bat algorithm [47] is one of the metaheuristic approaches inspired by the echolocation behavior of bats and based on swarm intelligence.

When hunting, the bat emits short, loud acoustic pulses, and then analyzes the echo to determine the size and location of an obstacle or prey. Observing this behavior, *Xin-She Yang* [48] proposed the standard BAT algorithm which can be clarified by the following:

(1) Initialization of the bat population and assignment to each individual i of the position (x_i), the velocity (v_i), the pulse frequency (f_i), the pulse rate (r_i) and the loudness (A_i).
(2) For i^{th} bat, update the global best position (x^*), f_i, v_i, and x_i, as follows:

$$\begin{cases} f_i = f_{\min} + (f_{\max} - f_{\min})\beta, \quad \beta \in [0,1] \\ v_i^{t+1} = v_i^t + (x_i^t + x^*) f_i \\ x_i^{t+1} = x_i^t + v_i^t \end{cases} \tag{28}$$

(3) A new solution is generated for the bat if the random number is greater than r_i:

$$x_{new} = x_{old} + \varepsilon A^t \tag{29}$$

where ε is a random number in $[-1, 1]$, and A^t represents the average loudness of all bats at time t.

(4) Accept the new solution if the random number is less than A_i and $f(x_i) < f(x^*)$, and therefore update A_i and r_i as follows:

$$\begin{cases} A_i^{t+1} = \alpha A_i^t \\ r_i^t = r_i^0 [1 - e^{-\gamma t}] \end{cases} \tag{30}$$

where f denotes the objective function and α and γ are constant parameters and are chosen as $0 < \alpha < 1$ and $0 < \gamma$, so that..$t \to \infty, A_i^t \to 0$, and $r_i^t \to r_i^0$.

(5) Find the current optimal solution (x^*) by sorting bats based on their fitness.
(6) Return to step 2 and once the maximum number of iterations is reached, output the optimal solution.

4.2.2. Deep feature

Due to the high correlation between images of healthy and diseased bones, the goal is to find feature vectors with high intra-class correlation and low inter-class correlation. In osteoporosis, bone tissue deteriorates often in depth, which is evident on 3D images. Sadly, in the case of 2D images, and in addition to the difficulties of the specialist detecting the disease with the naked eye, the handcrafted feature extraction approaches do not provide accurate and distinctive vectors for the automatic diagnosis.

Inspired by the advantages of deep analysis and Gabor's descriptor, we propose in this part a novel feature extraction method for the detection of osteoporosis. First, we'll filter the image using a Gabor filter bank (using certain orientations). Indeed, lines, wrinkles, ridges, singular points, and texture can all be detected in an image using a feature space based on the Gabor transform. This allows us to extract the bone features, especially the lines, from their respective backgrounds in the filtered image. Osteoporosis can be diagnosed by detecting a progressive change in the size, shape, and density of lines within an image of the bone. Then, we will combine all the filtered images into a single descriptor to reduce data amount, and finally we will use HOG/LPQ to extract the feature vector from the descriptor. Gabor Filter Bank parameters are adjusted, using Bat Algorithm Optimization, during training for accurate vectors. Fig. 2 contains a block diagram of the entire feature extraction process, including Gabor filtering, data reduction, and feature vector extraction.

This structure includes three main layers: the convolution layer, the pooling layer, and the feature vector extraction layer. In order to discuss the system's architecture, we will assume that the input images have the dimensions $H \times W$ and that the patch size, *i.e.* the size of the 2D convolutional filter, for the convolution layer is:

$$\mathscr{W}_{(n,\theta_i)} = k_1 \times k_2, \quad i \in [1..N] \tag{31}$$

where n is the scale number (in our work, $n = 1..8$), θ is the Gabor filter orientation (we employ 16 orientations from 0 to π, *i.e.* step of $\pi/16$), and N is the number of filters used. Noting that it is necessary to provide the system with the scale number and the number of filters, which can be less than eight filters, we will now describe how to choose the orientations of the filters.

- **Gabor filter orientations:** The purpose of the filtering process is to highlight the most important features of the image. Therefore, the choice of Gabor filter orientation is crucial and should be based on the type of features to be highlighted. In the image of bones shown in Fig. 3, the lines, which are often slanted vertically, are the most prominent feature.

In this figure, the lines run from top to bottom and are generally restricted to an angle of $90^o \pm 30^o$. Fig. 3.*(a)* represents an image with an orientation of approximately 75^o, while Fig. 3.*(c)* represents an image with an orientation of approximately 105^o, however the lines in the image of Fig. 3.*(b)* point in the orientation of 90^o.

In general, orientations are determined by the number of filters used, and vertical orientations always take precedence, as shown in Fig. 3.*(d)*.

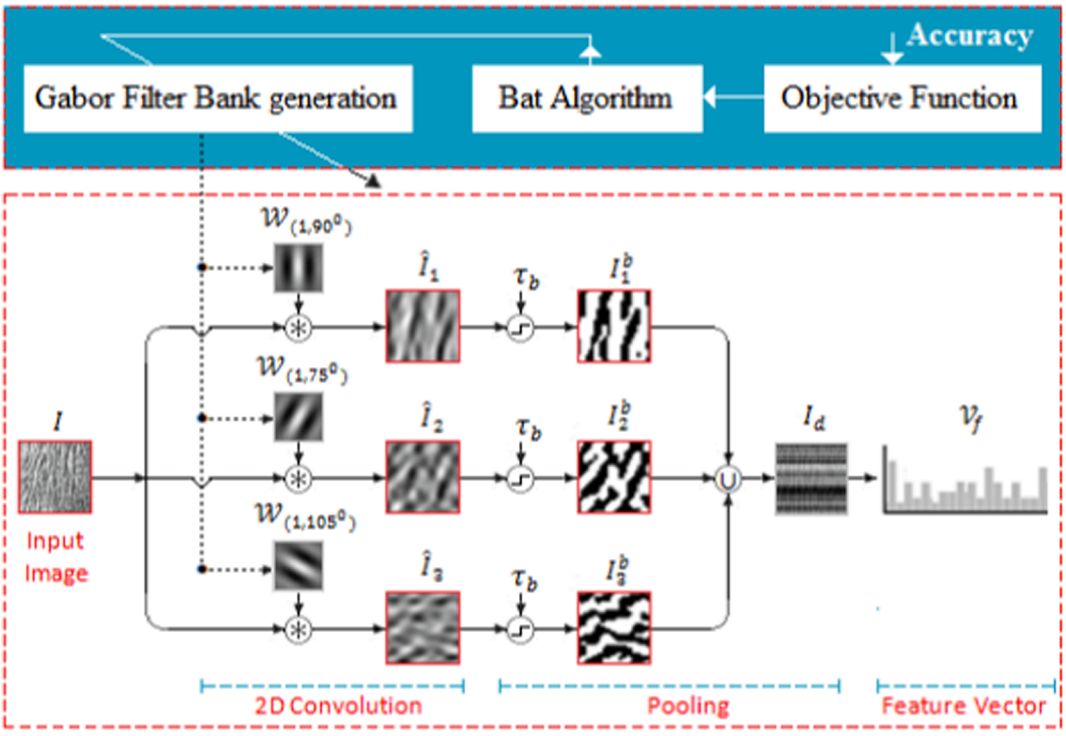

Fig. 2. Feature extraction. An example of a one-scale structure with three convolution filters of different orientations.

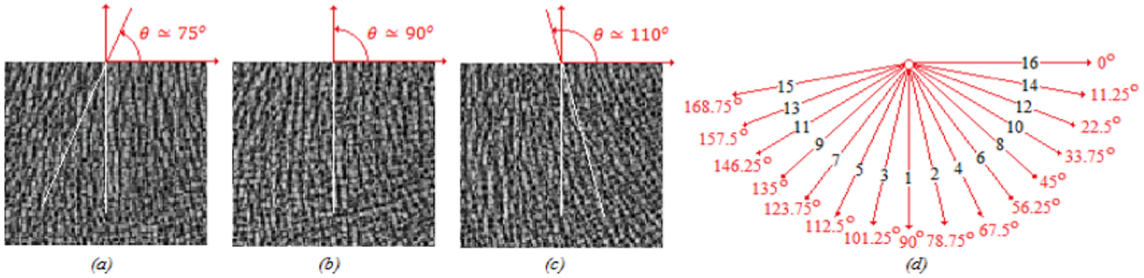

Fig. 3. Selection of the Gabor filters orientations. *(a)* The lines are in the first quarter, *(b)* Lines are usually vertical, *(c)* The lines are in the fourth quarter, and *(d)* The priority orientation.

Mathematically, if N is the number of Gabor filters, then each filter's orientation can be represented as follows:

If N odd:..$N = 2p + 1 \Rightarrow$

$$S_\theta = \{\theta_j\}_{j=0\cdots p}, \quad \theta_j = \frac{\pi}{2} \pm j\frac{\pi}{16}, \quad \text{and} \quad p = \frac{N-1}{2} \tag{32}$$

If N even:..$N = 2p \Rightarrow$

$$S_\theta = \{\theta_j\}_{j=0\cdots(p-1)} \cup \left\{\frac{\pi}{2} + \frac{N}{2}\frac{\pi}{16}\right\}, \quad \theta_j = \frac{\pi}{2} \pm j\frac{\pi}{16}, \quad \text{and} \quad p = \frac{N-1}{2} \tag{33}$$

We utilized an increment with a step of $\frac{\pi}{16}$; this step can be decreased or increased to improve the system's accuracy. Following the determination of the scale number and selection of the orientations of the filters, we will describe the functional behavior of our feature extraction method.

- **Functional Architecture:** In this part, we will see how the feature extraction function works to provide an accurate feature vector to maximize efficiency.

Convolution layer: The main purpose of a convolution layer is to enhance the dominant features of the input image. In addition to the orientation of the filter, its size (variance) also plays an important role, as it determines the size of the neighbors involved in the computation of each pixel's coefficient. The outputs of this layer are obtained by a 2D convolution process of all the images of the train database (Ψ_{train}) and the filters $\mathscr{W}_{(n,\theta_i)}$:

$$\widehat{I}_{ji} = I_j * \mathscr{W}_{(n,\theta_i)}, \quad i \in [1..N], \quad \theta_i \in S_\theta \quad j \in [1..N_{\text{train}}] \tag{34}$$

Where N_{train} denotes the number of images in Ψ_{train}, symbol * is the 2D convolution process, and $\widehat{I}_{ji}$ are the filtered output images.

Pooling layer: When N filters are applied to images, N additional images are produced, resulting in a significant increase in data. The pooling layer reduces the amount of data while keeping image features. Indeed, due to the fact that the relevant features have high and positive values, quantization can be used to find their location. in our work, we use the following linear threshold function:

$$I_{ji}^b(x,y) = \begin{cases} 0 & \text{if} \quad \widehat{I}_{ji}(x,y) < \tau_b \\ 1 & \text{if} \quad \widehat{I}_{ji}(x,y) \geq \tau_b \end{cases}, \quad i \in [1..N] \tag{35}$$

where τ_b is the threshold for binarization. In our work, we set this threshold to 0 because the coefficients of the filtered image $(\widehat{I}_i(x,y), \forall x, y)$ had the same probability of being negative or positive.

Next, the N-binarized images ($I_{ji}^{b}\big|_{i=1..N}$) are converted to an integer-valued image. Consequently, the N-binary codeword surrounding each pixel is transformed according to the following formula:

$$I_{jd}(x,y) = \sum_{i=1}^{N} I_{ji}^{b}(x,y)\cdot 2^{(i-1)} \tag{36}$$

As a result, we will get a single image to which we will apply a handcrafted feature extraction algorithm in order to extract its features.

Feature vector layer: In this step, a handcrafted feature extraction method (HOG and/or LPQ) is applied to the analyzed image (I_j) to extract the feature vector ($\mathscr{V}_I$).

$$\mathscr{V}_j^{\text{MTD}} = \mathscr{F}_{\text{MTD}}\left(I_{jd}\right), \quad \text{MTD} \equiv \{\text{HOG}, \text{LPQ}\} \tag{37}$$

Both methods (HOG and LPQ) have a variety of parameters that can be modified to control the size and precision of the feature vector.

In fact, the precision of this vector affects the effectiveness of the detection system; hence we selected and quantized its coefficients using the following formula during the training phase.

$$\widetilde{\mathscr{V}}_j = \mathscr{F}_{\text{QNTZ}}\left(\upsilon_j(x)\right) = \begin{cases} \upsilon_j(x) & \text{if} \quad \upsilon_j(x) \geq \lambda_0\cdot\rho_\upsilon \\ 0 & \text{Othrwise} \end{cases}, \quad \widetilde{\mathscr{V}}_j \in \mathbb{R}^{1\times L}, \quad x \in [1..L] \tag{38}$$

and

$$\upsilon_j = \mathscr{F}_{\text{SLCT}}\left(\mathscr{V}_j^{\text{MTD}}\right) \tag{39}$$

where υ_j represents the feature vector reorganized according to the coordinates obtained by the Fisher's selection method [49], which yields a vector with a predefined number of coordinates (L) in decreasing order of importance, ρ_υ is the average value of υ_j, and λ_0 is a predefined value.

- **Optimization:** To create a Gabor filter bank, it is necessary to provide three parameters (f_0, γ, and η). In our work and during the training phase, we employ the Bat algorithm optimization to find the optimal system performance-enhancing settings ($f_0^{\text{best}}0, \gamma^{\text{best}}$, and η^{best}).

$$\left[f_0^{\text{best}}0, \gamma^{\text{best}}, \eta^{\text{best}}\right] = \mathscr{F}_{\text{OPT}}\left(\text{S}_{\text{accuracy}}\right) \tag{40}$$

where $\text{S}_{\text{accuracy}}$, which is the system accuracy, represents the objective function.

4.3. Classifier

In classification problems, discriminative machine learning finds a function that can correctly identify instance labels. As one of the most important techniques in discriminative machine learning, the Support Vector Machines (SVM) [50] classifier finds the hyperplane (Eq. (41)) that correctly separates two classes with maximum margin.

$$g(x) = w^T x + b \tag{41}$$

Learning an SVM has been formulated as a *constrained* optimization problem that minimizes the following objective function:

$$J(w,b,\xi) = \frac{1}{2}\|w\|^2 + C\sum_{i=1}^{N}\xi_i \tag{42}$$

Subject to these constraints:

$$\begin{cases} y_i[x_i w_i + b] \geq 1 - \xi_i \\ \xi_i \geq 0 \end{cases}, \quad i = 1, 2, \cdots, N \tag{43}$$

where C denotes the margin size control parameter. The Lagrangian function for SVM is constructed by adding a weighted sum of the constraints to the objective function:

$$\mathscr{L} = \frac{1}{2}\|w\|^2 + C\sum_{i=1}^{N}\xi_i - \sum_{i=1}^{N}\alpha_i[y_i(x_i w_i + b) - 1 + \xi_i] - \sum_{i=1}^{N}\mu_i\xi_i \tag{44}$$

After executing the relevant processes, we get w and b, which determine the optimal hyperplane orientation:

$$w = \sum_{i=1}^{N}\alpha_i y_i x_i, \quad \text{and} \quad b = \frac{1}{N_s}\sum_{s\in S}\left(y_s - \sum_{m\in S}\alpha_m y_m x_m \cdot x_s\right) \tag{45}$$

Where S denotes the set of indices of the Support Vectors ($i/\alpha_i > 0$), and x_s represents the data point that satisfies $\sum_{i=1}^{N}\alpha_i y_i = 0$. Finally, each new point x_{new} is classified by evaluating the following formula:

$$y_{\text{new}} = \text{sgn}(w_i \cdot x_{\text{new}} + b) \tag{46}$$

5. Results

This section evaluates the proposed osteoporosis diagnosis system. We'll split the experiments into three parts. First, we'll thorough evaluation the proposed method, then determine the appropriate settings of our feature extraction method. In the last part, we'll evaluate the effect of the data fusion on system performance.

5.1. Construction of training and testing set

Our dataset contains 174 samples organized in three galleries. The first and second galleries were used to train the classifier, while the third gallery was used to evaluate the blind classification. To train the classifier using 10-fold cross-validation, the 116-sample dataset was randomly partitioned into 10 subsets, and 10 rounds of training and testing were conducted. After training the classifier and determining the optimal parameters of the proposed feature extraction method, the best model was selected and used to classify the remaining 58 blind samples.

5.2. Implementation

All experiments were performed with Matlab 2015a software on Windows 7 Professional and a SONY VAIO laptop model VPCEH2J1E with an Intel(R) Core(TM) i3-2330 M CPU running at 2.2 GHz and 6 GB of DRAM. In addition to the custom routines developed by the authors, we also used Matlab's built-in functions.

5.3. Performance

In this section, we will comprehensively evaluate the proposed method, from the normalization step to the fusing step, including the step of selecting the optimal parameters for the Gabor filters.

5.3.1. Preliminary assessment

The acquisition device provides 16-bit bone images. Before beginning the process of feature extraction, we first apply the Contrast Limited Adaptive Histogram Equalization (CLAHE) [51] approach to the region of interest to enhance the contrast of the bone images. Thus, the tile sub-region is one of the most important parameters of this method, so we'll explore three alternative tile sizes to determine which will produce the most enhanced image. To achieve this, we incorporated the enhanced images into an osteoporosis diagnosis model based on handcrafted feature extraction techniques (Filtering-free model). Our evaluation dataset consists of 400 × 400-pixel images, so we will explore tiles with medium-sized (20 × 20,40 × 40 and 80 × 80). Fig. 4 depicts the results for the three examined sizes using the two handcrafted feature extraction techniques (HOG and LPQ). The HOG method operates with cells of size 80 × 80 and produces a histogram with 9 bins, whereas the LPQ algorithm utilizes a window size of 15 × 15. Moreover, these two feature extraction methods are applied on the entire image.

The two graphs in this figure illustrate the system accuracy (ACC),

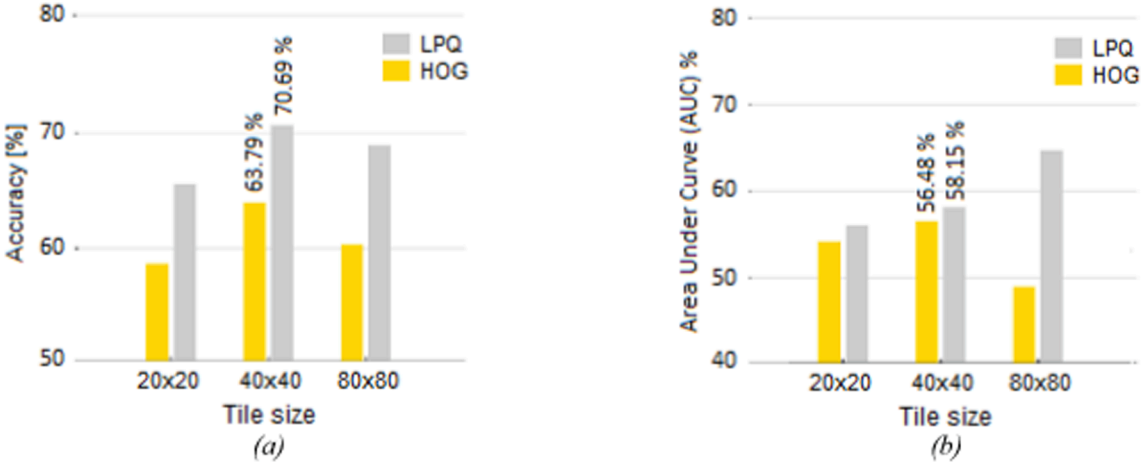

Fig. 4. Performance comparison under numerous CLAHE tile sizes. *(a)* System accuracy (ACC), and *(b)* Area under curve (AUC).

Fig. 4.*(a)*, and the Area Under the receiver operating characteristic (ROC) curve (AUC), Fig. 4.*(b)*, respectively. Consequently, from the different graphs in Fig. 4, two major observations can be drawn:

- In terms of ACC and AUC, the LPQ method outperforms the HOG method regardless of tile size.
- In general, 40 × 40-sized tiles showed the highest effectiveness.

For the HOG-based model, the performance in terms of (ACC, AUC) reaches (63.79%, 56.48%) at the decision threshold (T_d^{HOG}) of −0.1358, and a confusion matrix of $M_{conf}^{HOG}(TP, FP, TN, FN) = (17, 9, 20, 12)$ with a ($N_f^{HOG} = 51$ features and a $\lambda_0^{HOG} = 0.90$. Similarly, the LPQ-based model works with a (ACC, AUC) of (70.69%, 58.15%) at the T_d^{LPQ} equal to −0.3578, and a confusion matrix of $M_{conf}^{LPQ}(TP, FP, TN, FN) = (22, 10, 19, 7)$ with $(N_f^{LPQ}, \lambda_0^{LPQ}) = (16, 1.00)$. Indeed, in the case of LPQ, it appears from Fig. 4.*(b)* that the AUC achieved with 80x80 size tiles is superior to that obtained with 40 × 40 size tiles. To further demonstrate the superiority of 40 × 40 size tiles, Table 1 illustrates the specificity (SPE), sensitivity (SEN), and F1-score.

From this table, it is clear that in the case of LPQ, the tile of size 40 × 40 is superior to that of size 80 × 80 in terms of SPE and F1-score. Therefore, to normalize the dataset images, we will utilize 40 × 40 -sized tiles in the remaining experiments.

- **Block based analysis markedly improves performance:** In most visual systems, block-based image analysis has evolved as a processing paradigm over the past decade. It has been widely used in image processing, especially for data compression and pattern recognition. In block-based analysis, the image is divided into sub-images or smaller blocks. Indeed, the calculation time and the memory space required to perform image processing are crucial. Therefore, it is more convenient to perform processing on multiple sets of reduced data than on the entire image. In this part of the testing, the efficiency of block-based image analysis in the osteoporosis diagnostic system will be evaluated. Thus, in our experiments, we adopted the following strategy: For each block size of the set S_{BLK} ($S_{BLK} = \{100 \times 100, 200 \times 200, 300 \times 300\}$), the original image is divided into blocks with one of the four overlap rates (OLP) provided in S_{OLP} ($S_{OLP} = \{0\%, 25\%, 50\%, 75\%\}$). The ACC is then calculated after HOG/LPQ is performed on the blocks. For each feature extraction method, 12 tests can be conducted, and the parameters with the highest ACC values are chosen as the best settings. In Fig. 5, system performance (ACC) is plotted as a function of block size and block overlap for the two feature extraction methods.

Table 1
Performance for different CLAHE tile sizes.

CLAHE Tile size	HOG			LPQ		
	SPE (%)	SEN (%)	F_1-score (%)	SPE (%)	SEN (%)	F1-score (%)
20 × 20	37.93	79.31	65.71	48.28	82.0.76	70.59
40 × 40	58.62	68.97	65.57	75.86	65.52	69.09
80 × 80	82.76	37.93	48.89	68.97	68.97	68.97

By observing and analyzing Fig. 5.*(a)* and Fig. 5.*(b)*, we can see that: *(i)* In the case of HOG, block-based analysis greatly increased system performance (13.50% improvement) compared to whole image analysis. In the best-case scenario (100 × 100 and 0% overlap), the system can operate with (ACC, AUC) values of (72.41%, 62.19%) at $T_d^{HOG} = -0.1390$ and a confusion matrix of $M_{conf}^{HOG} = (15, 2, 27, 14)$ with (N_f^{HOG}, λ_0^{HOG}) values of (11, 1.00), and *(ii)* A block size of 100 × 100 is still better even in the LPQ, but with a 75% overlap, in which an ACC improvement of about 7.32% was obtained. Thus, the system can operate with (ACC, AUC) values of (75.86%, 71.34%) at $T_d^{LPQ} = 0.4441$ and a confusion matrix of $M_{conf}^{LPQ} = (24, 9, 20, 5)$ with (N_f^{LPQ}, λ_0^{LPQ}) values of (41, 0.75). Additional results of block-based image analysis are shown in Table 2.

Previous tests were conducted without the filter layer (filtering-free), during which the size of each CLAHE tile and analysis block was determined. Future experiments will include the filtering layer to assess the impact of this layer on system performance.

- **Filtering input image markedly improves performance:** After having normalized the image using a previously determined CLAHE tile, each block of size 100 × 100 will be filtered using a set of Gabor filters to obtain numerous descriptors. After combining these descriptors, a HOG/LPQ will then be applied to the resulting combination, and the obtained vectors will be concatenated to form a feature vector. The block was analyzed using N Gabor filters ($N \in [2, 3, .., 8]$) of three distinct sizes ($k_1 \times k_2 \equiv \{3 \times 3, 5 \times 5, 7 \times 7\}$). Notably, the initial values of f_0, γ and η for the Gabor filters have been chosen randomly, and to limit the number of tests, only the first scale of the Gabor filter bank is used.

GBR-HOG based osteoporosis diagnosis system: In the Gabor-HOG (GBR-HOG)-based system, f_0, γ and η were randomly assigned the values 0.637, 0.921, and 0.834, respectively. Since varying the number/size of the Gabor filter (N and $k_1 \times k_2$) produces different feature representations, we can experimentally select a (N, $k_1 \times k_2$) combination

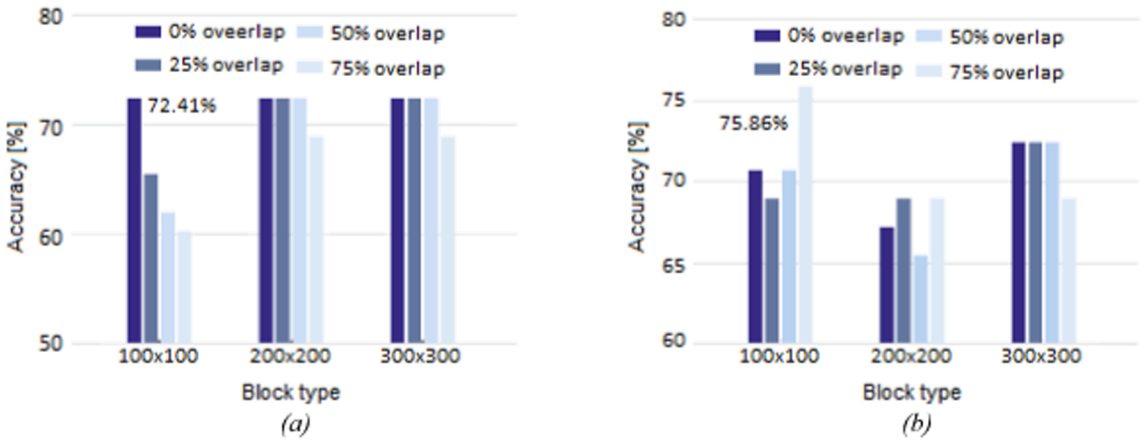

Fig. 5. Comparison of performance based on ACC using a variety of analysis block sizes. *(a)* HOG based osteoporosis diagnostic system, and *(b)* LPQ based osteoporosis diagnostic system.

Table 2
Performance for different analysis block sizes.

Analysis	HOG				LPQ			
Block type	SPE (%)	SEN (%)	AUC (%)	OLP (%)	SPE (%)	SEN (%)	AUC (%)	OLP (%)
100×100	51.72	93.10	62.19	0	82.76	68.97	71.34	75
200×200	58.62	86.21	64.80	0	72.41	65.52	63.02	25
300×300	72.41	72.41	68.61	0	79.31	65.52	77.05	0

that improves the system's accuracy. In order to understand the effect of these parameters, Fig. 6 shows the ACC results as a function of the number of filters (N) for all filter sizes ($k_1 \times k_2$).

This figure clearly demonstrates that the small size of the filter gives better results when the number of filters increases, while the large size gives better results when the number of filters decreases. Thus, the highest ACC was generated by two $7\times$ 7-sized filters ($\theta = \{90^o, 101.25^o\}$) or eight $3\times$ 3-sized filters ($\theta = \left\{90^o \pm 11.25^o j|_{j=0..3}, 135^o\right\}$). Obviously, two 7x7-sized Gabor filters with a confusion matrix of $M_{\text{conf}}^{\text{GBR}-\text{HOG}} = (22, 6, 23, 7)$ and ($N_f^{\text{GBR}-\text{HOG}}$, $\lambda_0^{\text{GBR}-\text{HOG}}$) values of (15, 0.25) are the optimal configuration in terms of processing time. Fortunately, it is evident that incorporating the filtering layer results in a 7.15 % improvement in system performance over the filtering-free configuration. Finally, it should be noted that these results are related to certain values of the Gabor filter's parameters (f_0, γ and η), suggesting that they can be improved by varying these parameters' values. Table 3 summarizes the overall results for the best case obtained.

GBR-LPQ based osteoporosis diagnosis system: Similarly, in the Gabor-LPQ (GBR- LPQ)-based system, f_0, γ and η were randomly assigned the values 0.898, 0.700, and 0.334, respectively. Fig. 7 shows the ACC results as a function of the number of filters (N) for all filter sizes ($k_1 \times k_2$).

The results in this figure show that the performance of our system generally improved (by more than 75%) only when we used a Gabor filter of size $3\times$ 3. Regarding ACC, it is evident that using 8 filters resulted in a 2.28% improvement in system performance. In this case, the system operates with an ACC of 77.59% and an AUC of 74.67%. The resulting confusion matrix is $M_{\text{conf}}^{\text{GBR}-\text{LPQ}} = (23,7,22,6)$, while the values of ($N_f^{\text{GBR}-\text{LPQ}}$, $\lambda_0^{\text{GBR}-\text{LPQ}}$) are (11, 0.70). Also, Table 3 summarizes the overall results for the best case obtained.

Finally, in order to demonstrate the importance of incorporating the filtering layer, we compare the best results obtained with those obtained without filtering layer (filtering-free) in Fig. 8.

This figure demonstrates the feasibility of the presence of this layer in the two cases, which greatly improved system performance, allowing the ACC to exceed 77%. Finally, it should be mentioned that it is feasible

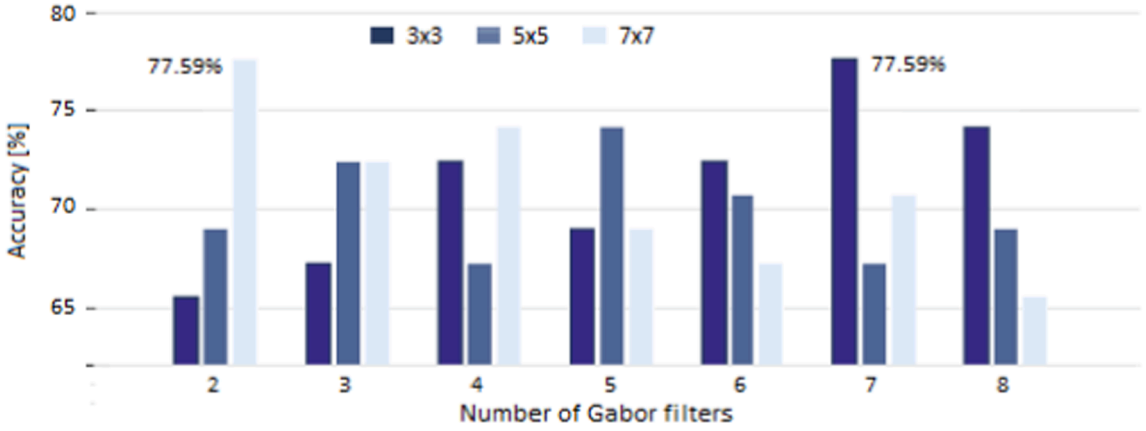

Fig. 6. Performance comparison of HOG-based system regarding ACC using a variety of Gabor filter numbers/sizes.

Table 3
System performance for effectively realized configurations (GBR-HOG and GBR-LPQ).

Methods	N	$\mathscr{W}$	T_d	SPE (%)	SEN (%)	AUC (%)	F1-score (%)	N_f	λ_0
GBR-HOG	2	3 × 3	0.0493	75.86	79.31	71.22	77.97	15	0.25
GBR-LPQ	8	3 × 3	−1.0054	79.31	75.86	74.67	77.19	11	0.70

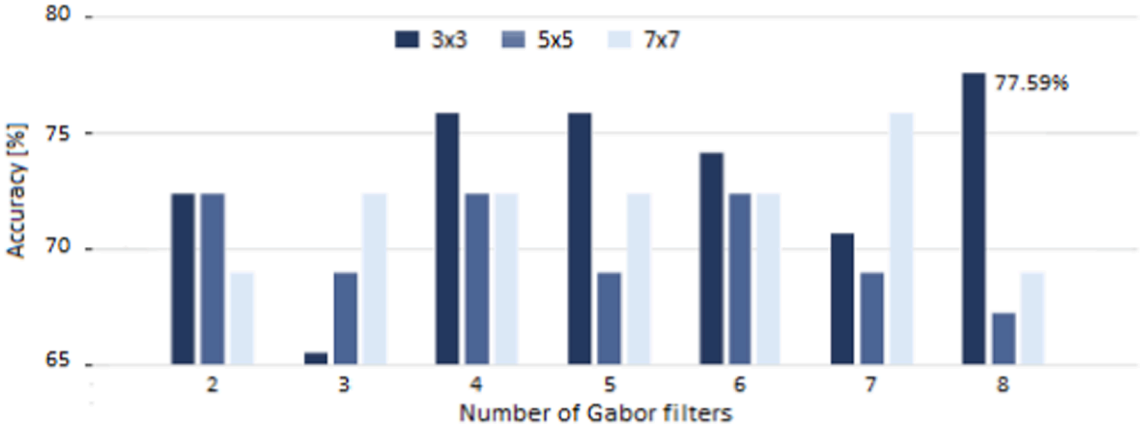

Fig. 7. Performance comparison of LPQ-based system regarding ACC using a variety of Gabor filter numbers/sizes.

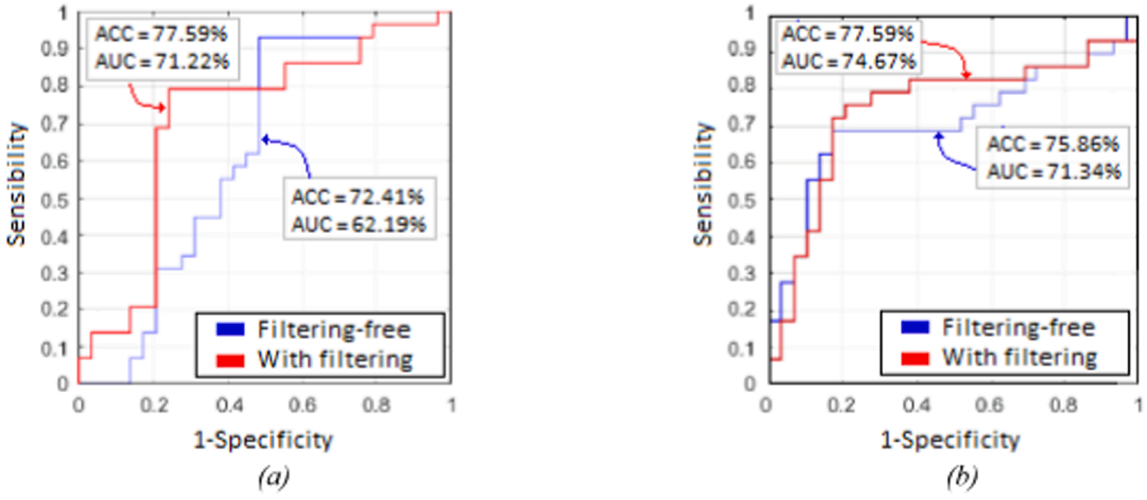

Fig. 8. Performance comparison between systems with and without a filtering layer. *(a)* HOG and GBR-HOG based osteoporosis diagnosis system, and *(b)* LPQ and GBR-LPQ based osteoporosis diagnosis system.

to improve these performances, as the HOG and LPQ techniques contain numerous parameters that, with careful selection, can be used to enhance the effectiveness of the osteoporosis diagnosis system.

5.3.2. Impact of optimizer on model performance

In previous experiments, the Gabor parameters (the digital frequency (f_o) and the two normalized scales (γ,η)) were randomly selected for the HOG and LPQ feature extraction methods. In this part, we will attempt to determine the optimal values for these parameters in order to achieve the best performance. In these tests, we do not limit the optimization to the best configurations mentioned above; rather, we will look for the optimal values using all available configurations, that is, for n, values ranging from 2 to 8 and the three filter sizes previously used. Therefore, we limit the search area of these parameters to the range of 0 to 1. The optimal results obtained after running the optimization algorithm are shown in Table 4.

From this table, in comparison with the previous results, we can easily see that the optimization process improved the system performance by 4.45% and 2.22% for GBR-HOG and GBR-LPQ respectively. It is clear that in both cases, 2 Gabor filters of size 3x3 gave the best results. In the case of the GBR-HOG and for the optimal parameters of the Gabor filter (0.730, 0.801, 0.619), the system works with values (ACC, AUC) of

Table 4
System performance at optimal Gabor filter settings.

Methods	N	$\mathscr{W}$	T_d	SPE (%)	SEN (%)	ACC (%)	AUC (%)	F_1-score (%)	N_f	λ_0
GBR-HOG	2	3 × 3	0.1565	86.21	75.86	**81.03**	80.86	80.00	61	0.30
GBR-LPQ			0.3775	93.10	65.52	**79.31**	75.86	76.00	46	0.10

(81.03%, 80.86%) at $T_d^{GBR-HOG} = 0.1565$ and a confusion matrix of $M_{conf}^{GBR-LPQ} = (25, 7, 22, 4)$, with ($N_f^{GBR-HOG}$, $\lambda_0^{GBR-HOG}$) values of (61, 0.30). In the case of GBR-LPQ feature extraction method, the optimal parameters of the Gabor filter were (0.880, 0.701, 0.719) and the system can operate with (ACC, AUC) values of (79.31%, 75.86%) at $T_d^{GBR-LPQ} = -0.3775$ and a confusion matrix of $M_{conf}^{GBR-LPQ} = (27, 10, 19, 2)$ with ($N_f^{GBR-LPQ}$, $\lambda_0^{GBR-LPQ}$) values of (46, 0.10), In order to demonstrate the significance of the optimization process, we compared the optimal results to those obtained without optimization in Fig. 9.

These two figures show the impact of the optimization procedure on system performance. It should also be remembered that another optimization algorithm can be used, such as Genetic Algorithm (GA) [52] or Particle Swarm Optimization (PSO) [53], and search in a wide range to improve filter parameters of Gabor.

5.3.3. Impact of data fusion on model performance

With diagnostic systems that only use information obtained from a single source, we cannot guarantee an accurate diagnosis. In fact, the error rates associated with these systems are rather significant, making their decisions unreliable. Creating multi-source diagnostic systems using lots of information extracted from the input image can overcome this challenge. Consequently, the purpose of this part is to explore whether the system performance might be improved by combining several information derived from the bone sub-image.

Pattern recognition systems have many sources of information that can be combined to improve their efficiency. In fact, this combination is performed according to the data fusion principle [54] which is a technique used to process information from multiple sources. It consists in combining data from several sources in order to obtain a better decision than that obtained from each source separately. In general, data fusion is the process of integrating several data in order to extract new information that is more representative of all the data.

In a multi-source system, there are many possible scenarios for the sources of information that can be considered. In our work, we have adopted multi-algorithm scenario, in which the bone image is independently analyzed using HOG and LPQ algorithms, and the resulting information is then fused to improve system performance. In this scenario, the fusion process can only be combined at three distinct levels: at feature level, at matching score level, or at decision level.

- **Feature level:** At this level, various feature vectors (observations) produced from the processing step (feature extraction step) are fused. Feature-level fusion can be implemented using a variety of techniques described in the literature. In our work, we implemented feature-level fusion using the Average (*AVR*), Concatenation (*CAT*), Canonical Correlation Analysis (*CCA*) [55], and Discriminant Correlation Analysis (*DCA*) techniques [56].

Let $\mathscr{V}_{HOG} = \mathscr{F}_{HOG}(I_i)$ and $\mathscr{V}_{LPQ} = \mathscr{F}_{LPQ}(I_i)$ be the feature vectors obtained from the bone sub-image I_i using the HOG and LPQ based feature extraction methods respectively. The resulting fused feature vector ($\mathscr{V}_{FUS}$) is defined as:

Average: in this case $\mathscr{V}_{HOG}$ and $\mathscr{V}_{LPQ}$ must be the same length.

$$\mathscr{V}_{FUS} = \frac{1}{2}(\mathscr{V}_{HOG} + \mathscr{V}_{LPQ}) \tag{47}$$

Concatenation (CAT):

$$\mathscr{V}_{FUS} = [\mathscr{V}_{HOG}, \mathscr{V}_{LPQ}] \tag{48}$$

In CCA and DCA, feature-level fusion is performed either by concatenation or by summation of the transformed feature vectors:

Canonical Correlation Analysis (CCA):

$$\mathscr{V}_{FUS} = W_{HOG}^T \bullet \mathscr{V}_{HOG} + W_{LPQ}^T \bullet \mathscr{V}_{LPQ} \text{ or } \left[W_{HOG}^T \bullet \mathscr{V}_{HOG}, W_{LPQ}^T \bullet \mathscr{V}_{LPQ}\right] \tag{49}$$

Discriminant Correlation Analysis (DCA).

$$\mathscr{V}_{FUS} = W'^T_{HOG} \bullet \mathscr{V}_{HOG} + W'^T_{LPQ} \bullet \mathscr{V}_{LPQ} \text{ or } \left[W'^T_{HOG} \bullet \mathscr{V}_{HOG}, W'^T_{LPQ} \bullet \mathscr{V}_{LPQ}\right] \tag{50}$$

where W_{HOG}^T, W_{LPQ}^T, W'^T_{HOG}, and W'^T_{LPQ} denote the transformation matrices (for more details see [57]).

- **Matching score level:** At this level, the individual scores are fused into a single score, which is then used to make the ultimate decision. Matching score-level fusion is the most common sort of fusion since it can be applied to all types of systems using simple and effective techniques. There are various techniques for combining scores (fusion rules) [58]. Indeed, the sum of the scores (SUM), the minimum of the scores (MIN), the maximum of the scores (MAX), and the product of the scores (MUL) are the rules most frequently employed.

Let d_{HOG} and d_{LPQ} be the matching scores obtained by the classification subsystems S_{HOG} and S_{LPQ}, the fused score (d_{FUS}) is computed by:

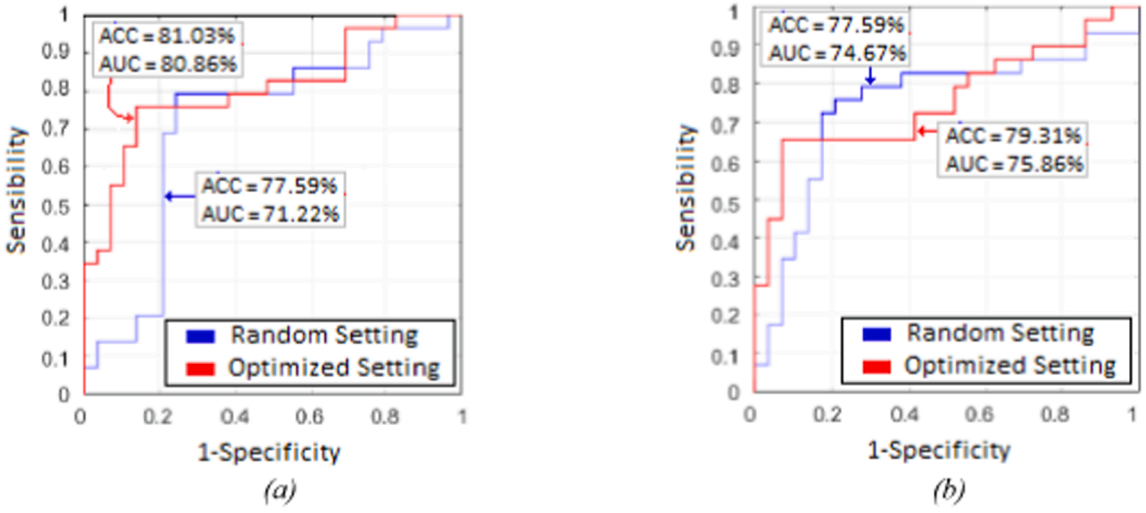

Fig. 9. Performance comparison between systems with and without a optimization. *(a)* HOG and GBR-HOG based osteoporosis diagnosis system, and *(b)* LPQ and GBR-LPQ based osteoporosis diagnosis system.

$$\textbf{\textit{SUMrule}} : d_{\mathrm{FUS}} = d_{\mathrm{HOG}} + d_{\mathrm{LPQ}} \tag{51}$$

$$\textbf{\textit{MAXrule}} : d_{\mathrm{FUS}} = \max(d_{\mathrm{HOG}}, d_{\mathrm{LPQ}}) \tag{52}$$

$$\textbf{\textit{MINrule}} : d_{\mathrm{FUS}} = \min(d_{\mathrm{HOG}}, d_{\mathrm{LPQ}}) \tag{53}$$

$$\textbf{\textit{MULrule}} : d_{\mathrm{FUS}} = d_{\mathrm{HOG}} \bullet d_{\mathrm{LPQ}} \tag{54}$$

It is important to note that these combination rules can only be applied if the scores of all subsystems are homogeneous. Consequently, an initial step of *scores normalization* is required.

– **Decision level:** At this level, the various decisions of the subsystems are combined in a single decision [59]. In fact, each subsystem provides a binary decision in the form of *'true'* or *'false'*, and the decision fusion step is to make a final decision based on this series of *'true'* or *'false'*. AND, OR and majority voting (VOTE) are the simplest principles for combining these decisions.

Let $S_i^{\mathrm{HOG}}|_{i=1}^{N}$ be a set of N HOG-based classification subsystems that use N different filter sizes, and let d_i^{HOG} be the decisions provided by the different classification subsystems, the fused decision ($d_{\mathrm{FUS}}^{\mathrm{HOG}}$) is computed by:

$$\textbf{\textit{ANDrule}} : d_{\mathrm{FUS}}^{\mathrm{HOG}} = \&_{i=1}^{\mathrm{N}} d_i^{\mathrm{HOG}} = d_1^{\mathrm{HOG}} \& d_2^{\mathrm{HOG}} \& \bullet\bullet\bullet \& d_N^{\mathrm{HOG}} \tag{55}$$

$$\textbf{\textit{ORrule}} : d_{\mathrm{FUS}}^{\mathrm{HOG}} = \|_{i=1}^{\mathrm{N}} d_i^{\mathrm{HOG}} = d_1^{\mathrm{HOG}} \left\| d_2^{\mathrm{HOG}} \right\| \bullet\bullet\bullet \left\| d_N^{\mathrm{HOG}} \right. \tag{56}$$

$$\textbf{\textit{VOTErule}} : d_{\mathrm{FUS}}^{\mathrm{HOG}} = \begin{cases} 1 & \text{if } N_{\mathrm{True}} \geq \left\lceil \dfrac{N}{2} \right\rceil \\ 0 & \text{Otherwise} \end{cases} \tag{57}$$

where N_{True} denotes the number of classification sub-systems with decision 1 ('*true*'), and the symbol $\lceil \alpha \rceil$ denotes the smallest integer that is not less than α.

By using all available configurations, it is possible to have several single-source subsystems. Consequently, our test will be limited to selecting the optimal configuration already obtained for all filter sizes for the GBR-HOG and GBR-LPQ based feature extraction methods. So, in order to find which fusion technique yields the highest ACC, Table 5 was generated for three fusion levels.

As this table shows, it was only by using fusion at the decision level that the performance of the osteoporosis diagnostic system was significantly improved. Indeed, fusing the information obtained by analyzing the image using all filter sizes according to the LPQ and the VOTE rule leads to a significant improvement in system performance. In this case, the system operates with an ACC equal to 89.66%, with an improvement of 26.85% compared to the primary system. The three fused subsystems keep the same decision thresholds ($T_{\mathrm{d}}^{\mathrm{GBR-LPQ}}$) and the same number of selected features ($N_f^{\mathrm{GBR-LPQ}}$), resulting in a confusion matrix $M_{\mathrm{conf}}^{\mathrm{FUSION}}$ equal to (25, 2, 27, 4). At the score-fusion level, the osteoporosis diagnostic system either retains the same performance as the uni-source system or degrades.

6. Discussion

In this part, we will attempt to present and discuss the major findings and provide some recommendations. In addition, a comparative study with relevant prior research will be presented.

6.1. Major findings

This paper explores the use of texture analysis to distinguish between healthy and osteoporotic bones. We have found that applying handcrafted feature extraction techniques directly to bone images does not yield encouraging results, as opposed to applying these techniques to descriptors derived through deep image analysis. Fig. 10 illustrates the difference between the two aforementioned methods.

From this figure it can be deduced that:

– Bone deterioration may be localized in a specific portion of the analyzed area; therefore, it is recommended to analyze the image block by block in order to decrease the inter-correlation ratio (between images of healthy and diseased bone). This strategy would decorrelate the feature vectors in a substantial portion of the vector coefficients at least.
– Practically, the filtering procedure will eliminate all unnecessary traits. In the bone image, the image lines are the most essential traits, so filters that can increase the contrast of these traits should be applied in order to effectively extract their features.
– It is crucial to link the classifier to the feature extraction method. In this scenario, the classifier plays the role of an expert, who will choose the parameters of the feature extraction method to improve its performance (deep behavior).

Table 5
Multi-source osteoporosis diagnostic system performance.

Fusion Level	GBR-HOG	GBR-LPQ	3 × 3	5 × 5	7 × 7	RULE	SPE (%)	SEN (%)	ACC (%)	AUC (%)	F_1-score (%)
FEATURE	×		×		×	CCA	75.86	72.41	74.14	66.83	73.68
	×			×	×	CAT	72.41	72.41	72.41	73.01	72.41
	×		×		×	AVR	72.14	72.41	72.41	69.80	72.41
		×	×		×	CAT	75.86	65.52	70.69	68.85	69.09
		×		×	×	AVR	68.97	72.41	70.69	70.63	71.19
	×	×	×			CCA	79.31	65.52	72.41	65.99	70.37
	×	×	×			DCA	79.31	60.07	75.00	65.87	67.92
	×	×		×		DCA	55.17	86.21	70.69	58.86	74.63
SCORES	×		×	×		MIN	82.76	72.41	77.59	78.48	76.36
	×		×		×	SUM	79.31	79.31	79.31	78.24	79.31
	×			×	×	SUM	72.41	82.76	77.59	78.69	78.69
		×	×	×		MIN	86.21	68.97	77.59	77.29	75.47
		×	×		×	MAX	68.97	82.76	75.86	73.01	77.42
		×		×	×	SUM	75.86	75.86	75.86	75.03	75.86
	×	×	×			SUM	72.41	82.76	77.59	74.91	78.69
	×	×		×		SUM	82.76	72.41	77.59	75.98	76.36
	×	×			×	MAX	75.86	75.86	75.86	79.79	75.86
DECISION	×		×	×	×	VOTE	88.46	81.25	84.48	/	85.25
		×	×	×	×	**VOTE**	**92.59**	**87.10**	**89.66**	/	**90.00**
	×	×	×			OR	95.00	73.68	81.04	/	83.58
	×	×		×		AND	68.42	85.00	74.18	/	69.39
	×	×			×	OR	100.00	69.05	77.59	/	81.69

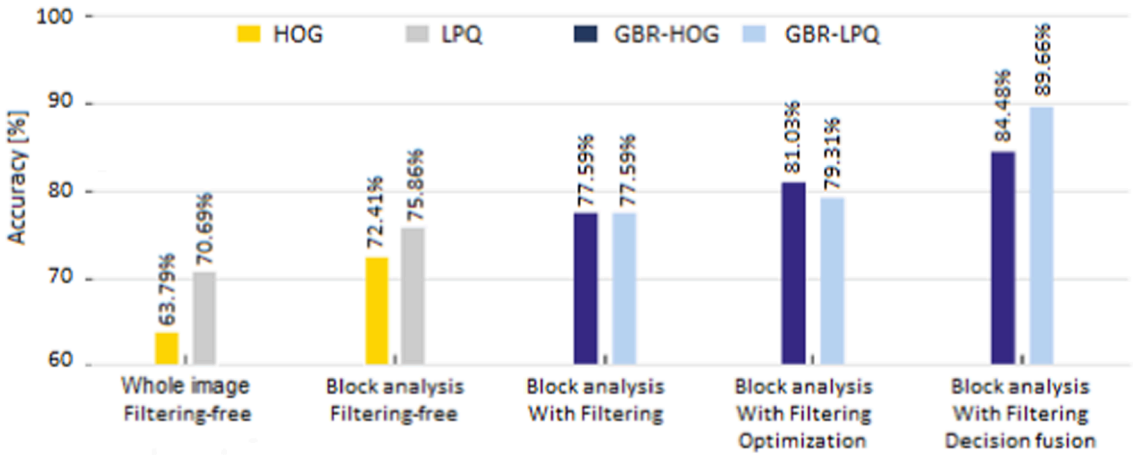

Fig. 10. The progress of improving system performance (the most significant results achieved).

– Given the significant correlation between healthy and diseased bone images, analyzing the image using many techniques and combining their results will improve system performance due to the additional data offered by each analysis process.

Lastly, it should be highlighted that there is still much work to be done to improve the performance of this system, for example by adopting feature-level fusion and pyramid analysis.

6.2. Comparison to previous methods

In the development of pattern recognition systems, it is essential to compare the results with those of previous research. To ensure a fair comparison, only works that used the same dataset and evaluation protocol will be chosen. In this part, in order to show the efficiency of our proposed method compared to existing methods (handcrafted /based deep learning), a comparative study with some recent works is carried out using the dataset provided by IEEE-ISBI Challenge, where the main works are summarized in Table 6.

This table clearly demonstrates the effectiveness of the proposed osteoporosis diagnostic system, as our system, whether based on a single source or multi-sources, outperforms all the methods listed in the table in terms of ACC (up to 89.66%) and AUC (up to 80.86%), allowing its use in Computer Aided Diagnosis (CAD).

7. Conclusion

Recent increases in the need for radiologists are primarily due to the rapid growth of medical imaging due to advancements in imaging technologies. Indeed, following the increase in demand, the workload of the radiologist has increased, which can unfortunately lead to diagnostic errors due to the specialists workload. Recently, the application of Artificial Intelligence (AI) approaches to the clinical practice of medical imaging has played a significant role in enhancing diagnostic accuracy and efficacy. In addition to improving diagnostic accuracy, these strategies bridge the gap between inexperienced and experienced clinicians or between generalists and specialists. The diagnosis of osteoporosis is one of the most crucial diagnostic practices requiring medical imaging. In this paper, we present an AI-based technique for automatically detecting osteoporosis by analyzing X-ray images of bone tissue. In this study, we developed a model for diagnosing osteoporosis based on handcrafted features taken from descriptors obtained from a thorough analysis of the bone image using a set of Gabor filters with different orientations. Two well-know hand-crafted methods were used to extract descriptor features, namely HOG and LPQ. To achieve a high level of performance, we used a bat-based optimization method to determine appropriate Gabor filter parameters. Additionally, we combined information at two distinct levels, including fusion at score level and fusion at decision level. In this study, we have attempted to cover all aspects of system development. Consequently, our studies consisted of selecting the optimal parameters of the normalization approach, deciding whether to analyze the full image or to analyze it in blocks, selecting the Gabor filter parameters, and lastly combining the information from various subsystems. In fact, all of these tests resulted in an excellent performance (ACC = 89.66%) that outperformed several previously published studies. In future work, we intend to combine these features with clinical data to develop a multimodality model. In addition, we will try to use/develop more predictive handcrafted features to improve the

Table 6
Performance comparison to some works in the state-of-the-arts.

Authors	Methods	Classifier	ACC (%)	SEN (%)	SPE (%)	AUC (%)	F1-score (%)
Yang et al. 2015, [39]	SIFT-IFV	SVM	68.00	72.00	66.00	68.00	63.90
	LBP-IFV		68.50	70.00	64.00	64.00	68.40
Florian Yger, 2014, [41]	Haar	SVM	64.00	62.00	66.00	–	63.90
Su et al. 2020, [15]	AlexNet + ECD[1]	SVM	77.50	74.70	83.30	82.10	76.40
Su et al. 2018, [26]	FS[2]	SVM	71.20	73.30	69.00	–	71.00
Palanivel et al. 2020, [22]	LH[3]	SVM	59.00	59.00	59.00	–	–
Proposed	Gabor-HOG	SVM	81.03	75.86	86.21	80.86	80.00
	Gabor-LPQ		79.31	65.52	93.10	75.86	76.00
	Decision fusion (HOG)		84.48	81.25	88.46	–	85.25
	Decision fusion (LPQ)		89.66	87.10	92.59	–	90.00

[1] ECD: Encoded features provided by: Gabor-GLCM (GGLCM) + Hessian- GLCM (HGLCM) + Local Gabor binary patterns (LGBP) + Local Hessian binary patterns (HLBP).
[2] FS: Feature selection from: GGLCM + LHBP + LGBP.
[3] LH: Lacunarity computed from the Hausdorff dimensions.

accuracy of the diagnosis.

Declaration of Competing Interest

The authors declare that they have no known competing financial interests or personal relationships that could have appeared to influence the work reported in this paper.

Data availability

The authors do not have permission to share data.

Acknowledgments

The authors are grateful to the anonymous referees for their valuable and helpful comments. This research has been carried out within the PRFU project (Grant: A01L08UN120120220001) of the Department of Electrical Engineering, University of Larbi Tebessi, Tebessa. The authors thank the staff of LAMIS laboratory for helpful comments and suggestions.

References

[1] E.B. Marcia, C. Javitt, Medical imaging: from roentgen to the digital revolution, and beyond, Rambam Maimon. Med. J. 9 (4) (2018) e0034.
[2] E.M. Lochmüller, N. Krefting, D. Bürklein, F. Eckstein, Effect of fixation, soft-tissues, and scan projection on bone mineral measurements with dual energy, X-ray absorptiometry (DXA), Calcif. Tissue Int. 68 (2001) 140–145.
[3] M. Adams, W. Chen, D. Holcdorf, M.W. McCusker, P.D.L. Howe, F. Gaillard, Computer vs. human: deep learning versus perceptual training for the detection of neck of femur fractures, J. Med. Imaging Radiat. Oncol 63 (2019) 27–32.
[4] Patil, Maya Deoker, Osteoporosis detection by using CT images based on gray level co-occurrence matrix and rule based approach, Int. J. Sci. Res. Dev. 5(08) (2017) 2321–0613.
[5] Keni Zheng, Sokratis Makrogiannis, Bone texture characterization for osteoporosis diagnosis using digital radiography, in: 38th Annual International Conference of the IEEE Engineering in Medicine and Biology Society (EMBC), Orlando, FL, USA, 2016.
[6] N.J. Macintyre, A.L. Lorbergs, Imaging-based methods for non-invasive assessment of bone properties influenced by mechanical loading, Physiother Can. 64 (2) (2012) 202–215.
[7] A.K. Samantaray, A.D. Rahulkar, New design of adaptive Gabor wavelet filter-bank for medical image retrieval, IET Image Process. 14 (4) (2020) 679–687.
[8] Jorge Erazo-Aux, H. Loaiza-Correa, A.D. Restrepo-Giron, Histograms of oriented gradients for automatic detection of defective regions in thermograms, Appl. Opt. 58(13) (2019) 3620–3629.
[9] Kanika Kapoor, Shalli Rani, Munish Kumar, Vinay Chopra & Gubinder Singh Brar, 'Hybrid local phase quantization and grey wolf optimization based SVM for finger vein recognition, Multimedia Tools Appl. 80 (2021) 15233–15271.
[10] Texture Characterization of Bone radiograph images (TCB) challenge data. Available online in http://www.univ-orleans.fr/i3mto/data, (last access in 05/2018).
[11] Bone Health and Osteoporosis: A Report of the Surgeon General. US Department of Health and Human Services: Washington, DC, USA 87 (2004) 15–25.
[12] Mitchell, P.J., Fracture Liaison Services, The UK experience, Osteoporosis Int. 22 Suppl 3(S3) (2011) 487–494.
[13] S.M. Nazia Fathima, R. Tamilselvi, M. Parisa Beham, A survey on osteoporosis detection methods with a focus on X-ray and DEXA images, IETE J. Res. (2020), https://doi.org/10.1080/03772063.2020.1803771.
[14] M.F. Victor Sim, M. Stone, A. Johansen, W. Evans, Cost effectiveness analysis of BMD referral for DXA using ultrasound as a selective pre-screen in a group of women with low trauma Colles' fractures, Technol. Health Care 8 (2000) 277–284.
[15] S.u. Ran, T. Liu, C. Sun, Q. Jin, R. Jennane, Leyi Wei,"Fusing convolutional neural network features with hand-crafted features for osteoporosis diagnoses", Neurocomputing 385 (2020) 300–309.
[16] S. Sultan, Y. Bekeneva, A comparative analysis of a designed CNN and AlexNet for image classification on small datasets, in: D. Camacho, D. Rosaci, G.M.L. Sarné, M. Versaci (Eds.), Intelligent Distributed Computing XIV. IDC 2021, Studies in Computational Intelligence, vol 1026, Springer, Cham, 2022.
[17] Jiang, Z., Zou, K., Yao, J., Li, D., Cao, X., ''Improved VGG-16 Neural Network for Parameter Reduction'', Sun, X., Zhang, X., Xia, Z., Bertino, E. (eds) Advances in Artificial Intelligence and Security. ICAIS 2022. Communications in Computer and Information Science, vol 1586, Springer, Cham, 2022.
[18] V Sreejith, Thomas George, Detection of COVID-19 from Chest X-rays Using Resnet-50, Journal of Physics: Conference Series, Volume 1937, International Conference on Novel Approaches and Developments in Biomedical Engineering (ICNADBE 2021), Coimbatore, India, 2021.
[19] N. Hasan, Y. Bao, A. Shawon, Y. Huang, DenseNet convolutional neural networks application for predicting COVID-19 using CT image, SN Computer Science 2 (2021) 389.
[20] S. Aouat, I. Ait-hammi, I. Hamouchene, A new approach for texture segmentation based on the Gray Level Co-occurrence Matrix, Multimed. Tools Appl. 80 (2021) 24027–24052.
[21] Megha Agarwal, Amit Singhal, Identification of heart failure from cine-MRI images using pattern-based features, Data Image Processing for Automated Diagnosis of Cardiac Diseases, 2021, pp. 173–193.
[22] Dhevendra Alagan Palanivel, Sivakumaran Natarajan, Sainarayanan Gopalakrishnan, Rachid Jennane, Multifractal-based lacunarity analysis of trabecular bone in radiography, Compute. Biol. Med. 116 (2020) 103559.
[23] I.A. Sheipak, Hölder exponents of self-similar functions, Funct. Anal. Appl. 53 (2019) 51–60.
[24] L. Crone, L. Fishman, S. Jackson, Hausdorff dimension regularity properties and games, Israel J. Math. 248 (2022) 481–500.
[25] D. Sebők, L. Vásárhelyi, I. Szenti, R. Vajtai, Z. Kónya, Á. Kukovecz, Fast and accurate lacunarity calculation for large 3D micro-CT datasets, Acta Mater. 214 (2021) 1169701.
[26] Ran Su, Weijun Chen, Leyi Wei, Xiuting Li, Qiangguo Jin, Wenyuan Tao, Encoded texture features to characterize bone radiograph images, IN: 24th International Conference on Pattern Recognition (ICPR), Beijing, China, 2018, pp. 3856–3861.
[27] Q.i. Mao, S. Zhao, D. Tong, S.u. Shengchao, Z. Li, X. Cheng, Hessian-MRLoG: Hessian information and multi-scale reverse LoG filter for pulmonary nodule detection, Comput. Biol. Med. 131 (2021), 104272.
[28] S. Hediger, L. Michel, J. Näf, On the use of random forest for two-sample testing, Comput. Stat. Data Anal. 170 (2022), 107435.
[29] Muhammad Ijaz, Atiq ur Rehman, Mounir Hamdi, Amine Bermak, Recursive feature elimination with random forest classifier for compensation of small scale drift in gas sensors, in: IEEE International Symposium on Circuits and Systems (ISCAS), Seville, Spain, 2020.
[30] Keni Zheng and Sokratis Makrogiannis, Bone texture characterization for osteoporosis diagnosis using digital radiography, in: 38th Annual International Conference of the IEEE Engineering in Medicine and Biology Society (EMBC), Orlando, FL, USA, 2016, pp. 1034–1037.
[31] Feng-Jen Yang, An implementation of naive bayes classifier, in: International Conference on Computational Science and Computational Intelligence (CSCI), Las Vegas, NV, USA, 2018.
[32] Flora Amato, Nicola Mazzocca, Francesco Moscato, Emilio Vivenzio, Multilayer perceptron: an intelligent model for classification and intrusion detection, in: 31st International Conference on Advanced Information Networking and Applications Workshops (WAINA), Taipei, Taiwan, 2017.
[33] P. Barbrook-Johnson, A.S. Penn, Bayesian belief networks, Systems Mapping. Palgrave Macmillan, Cham, 2022.
[34] C.M. Akujuobi, Wavelet Transforms, Wavelets and Wavelet Transform Systems and Their Applications, Springer, Cham, 2022.
[35] W. Burger, M.J. Burge, The Discrete Cosine Transform (DCT), Digital Image Processing, Texts in Computer Science, Springer, Cham, 2022.
[36] G. Edgar, Fractal dimension, in: G. Edgar (Eds.), Measure, Topology, and Fractal Geometry, Undergraduate Texts in Mathematics, Springer, New York, NY, 2008.
[37] M.M. Farhangi, M. Soryani, M. Fathy, Improvement the bag of words image representation using spatial information, in: N. Meghanathan, D. Nagamalai, N. Chaki (Eds.), Advances in Computing and Information Technology, Advances in Intelligent Systems and Computing, vol. 177, Springer, Berlin, Heidelberg, 2013.
[38] Michalis A. Savelonas, Ioannis Pratikakis, Konstantinos Sfikas, Fisher encoding of differential fast point feature histograms for partial 3D object retrieval, Pattern Recogni. 55 (2016) 114–124.
[39] Yang Song, Weidong Cai, Fan Zhang, Heng Huang, Yun Zhou, David Dagan Feng, Bone texture characterization with fisher encoding of local descriptors, in: IEEE 12th International Symposium on Biomedical Imaging (ISBI), Brooklyn, NY, USA, 2015, pp. 5–8.
[40] Y. Li, W. Liu, X. Li, Q. Huang, X. Li, GA-SIFT: a new scale invariant feature transform for multispectral image using geometric algebra, Inf. Sci. 281 (2014) 559–572.
[41] Florian Yger, Challenge IEEE-ISBI/TCB: application of covariance matrices and wavelet marginals, arXiv: 1410.2663, 2014.
[42] M Kamaledin Ghiasi-Shirazi, Learning 2D Gabor filters by infinite kernel learning regression, J. Comput. Math. Data Sci. 1 (2021) 100016.
[43] V. Tadic, Z. Kiraly, P. Odry, Comparison of gabor filter bank and fuzzified gabor filter for license plate detection, Acta Polytech. Hungar. 17 (1) (2020) 61–81.
[44] W. Zhou, S. Gao, L. Zhang, X. Lou, Histogram of oriented gradients feature extraction from raw bayer pattern images, IEEE Trans. Circ. Syst. Exp. Briefs 67 (5) (2020) 946–950.
[45] Y. Xiao, Z. Cao, L.i. Wang, T. Li, Local phase quantization plus: a principled method for embedding local phase quantization into Fisher vector for blurred image recognition, Inf. Sci. 420 (2017) 77–95.
[46] V. Ojansivu, J. Heikkilä, Blur insensitive texture classification using local phase quantization, in: Proceedings of International Conference on Image and Signal Processing, 2008, pp. 236–243.
[47] Z.A.A. Alyasseri, O.A. Alomari, M.A. Al-Betar et al., Recent advances of bat-inspired algorithm, its versions and applications, Neural Computing and Applications, Neural Comput & Applic, 2022.
[48] Xin-She Yang, A new metaheuristic bat-inspired algorithm, in: J.R. Gonzalez et al. (Eds.), Nature Inspired Cooperative Strategies for Optimization (NISCO 2010), Studiesin Computational Intelligence, Springer Berlin, 284, Springer, 2010, pp. 65–74.

[49] R. Shang, Y. Meng, C. Liu, L. Jiao, A.M. Ghalamzan, R.S. Esfahani, Unsupervised feature selection based on kernel fisher discriminant analysis and regression learning, Mach. Learn. 108 (2019) 659–686.
[50] M Babacar Gaye, Dezheng Zhang, Aziguli Wulamu, "Improvement of Support Vector Machine Algorithm in Big Data Background", Mathematical Problems in Engineering, vol. 2021, Article ID 5594899, 2021.
[51] Suharyanto, Z.A. Hasibuan, P.N. Andono, D. Pujiono and R.I.M. Setiadi, Contrast limited adaptive histogram equalization for underwater image matching optimization use SURF, Journal of Physics: Conference Series, Vol. 1803, 2nd International Conference on Enhanced research and Industrial Application, Yogyakarta, Indonesia, 2020.
[52] V.K. Singh, K.C. Panda, et al., Novel Genetic Algorithm (GA) based hybrid machine learning-pedotransfer Function (ML-PTF) for prediction of spatial pattern of saturated hydraulic conductivity, Eng. Appl. Comput. Fluid Mech. 16 (1) (2022) 1082–1099.
[53] G.Gad Ahmed, Particle swarm optimization algorithm and its applications: a systematic review, Arch. Comput. Meth. Eng. 29 (2022) 2531–2561.
[54] M.A. Khan, T.M. Ghazal, S.-W. Lee, A. Rehman, Data fusion-based machine learning architecture for intrusion detection, Comput. Mater. Continua 70 (2) (2022) 3399–3413.
[55] Z. Wang, L. Wang, H.a. Huang, Sparse additive discriminant canonical correlation analysis for multiple features fusion, Neurocomputing 463 (2021) 185–197.
[56] M. Haghighat, M. Abdel-Mottaleb, W. Alhalabi, Discriminant correlation analysis for feature level fusion with application to multimodal biometrics, in: IEEE International Conference on Acoustics, Speech and Signal Processing (ICASSP), Shanghai, China, 2016, pp. 1866–870.
[57] M. Haghighat, M. Abdel-Mottaleb, W. Alhalabi, Discriminant correlation analysis: real-time feature level fusion for multimodal biometric recognition, IEEE Trans. Inf. Forensics Secur. 11 (9) (2016) 1984–1996.
[58] M. Saigaa, S. Chitroub, A. Meraoumia, An effective biometric identification system using enhanced palm texture features, Evol. Syst. 13 (2021) 43–63.
[59] H.O. Ihan, G. Serbes, N. Aydin, Decision and feature level fusion of deep features extracted from public COVID-19 data-sets, Appl. Intell. 52 (2022) 8551–8571.